Journal of Materials Science & Technology 83 (2021) 208–218

Contents lists available at ScienceDirect

Journal of Materials Science & Technology

journal homepage: www.jmst.org

Research Article

Thermal stability of additively manufactured austenitic 304L ODS alloy

Milad Ghayoor[a,b], Saereh Mirzababaei[a,b], Anumat Sittiho[c], Indrajit Charit[c], Brian K. Paul[a,b], Somayeh Pasebani[a,b,*]

[a] School of Mechanical, Industrial and Manufacturing Engineering, Oregon State University, Corvallis, OR, 97330, United States
[b] Advanced Technology and Manufacturing Institute (ATAMI), Corvallis, OR, 97330, United States
[c] Materials Science and Engineering, University of Idaho, Moscow, ID, 83844, United States

ARTICLE INFO

Article history:
Received 18 September 2020
Received in revised form
25 November 2020
Accepted 7 December 2020
Available online 26 January 2021

Keywords:
Laser powder bed fusion (LPBF)
Oxide dispersion strengthened (ODS) alloy
High-temperature
Aging
Thermal stability

ABSTRACT

Thermal stability and high-temperature mechanical properties of a 304L austenitic oxide dispersion strengthened (ODS) alloy manufactured via laser powder bed fusion (LPBF) are examined in this work. Additively manufactured 304L ODS alloy samples were aged at temperatures of 1000, 1100, and 1200 °C for 100 h in an argon atmosphere. Microstructure characterization of LPBF 304L ODS alloy before and after the thermal stability experiments revealed that despite the annihilation of dislocations, induced cellular substructure by the LPBF process was partially retained in the ODS alloy even after aging at 1200 °C. The size of Y-Si-O nanoparticles after aging at 1200 °C increased from 25 to 50 nm. EBSD analysis revealed that nanoparticles retained the microstructure of LPBF 304L ODS and hindered recrystallization and further grain growth. At 600 °C and 800 °C, the yield stress of the 290 and 145 MPa were measured, respectively, which are substantially higher than 113 MPa, and 68 MPa for 304L at the same temperatures. Furthermore, the creep properties of LPBF 304L ODS alloy were evaluated at a temperature of 700 °C under three applied stresses of 70, 85, and 100 MPa yielding a stress exponent (n) of ~7.7; the minimum creep rate at 100 MPa was found to be about two orders of magnitude lower than found in the literature for wrought 304L stainless steel.

1. Introduction

Additive manufacturing (AM) technologies enable the manufacturing of parts with complex geometry using a wide range of materials such as metals, ceramics, and polymers for various applications without the need for expensive tooling and machining [1–6]. Furthermore, AM technologies promise lower material consumption by recycling and reusing materials [7]. Laser powder bed fusion (LPBF) is a metal additive manufacturing process, offering a promising alternative to fabricate components with fine microstructure and improved mechanical properties due to an extremely high cooling rate (>10^4 °C/s) induced by the laser [8–12].

Ferritic and austenitic stainless steels (manufactured via the LPBF process) [1,13] do not possess a high creep resistance required for high-temperature environments. The oxide dispersion strengthening (ODS) mechanism can be adopted to enhance the creep and oxidation resistance [14]. The conventional manufacturing of ODS alloy is through complex powder metallurgy and mechanical alloying (MA) processes. The matrix powder and the highly stable nanoparticles, such as Y_2O_3, are mechanically alloyed using a high energy ball milling process. During MA, the Y_2O_3 nanoparticles are atomically dissociated, forming a supersaturated solid solution that will go through a precipitation mechanism forming complex oxide nanoparticles and clusters during a subsequent hot consolidation such as hot extrusion or hot isostatic pressing (HIP) [15–18]. An ultra-high number density of oxide nanoparticles pins dislocation movements and grain boundaries, hence stabilizing the microstructure at high temperatures making the investigation of thermal stability of ODS alloys of significant scientific and practical interest [19,20].

Conventionally manufactured ferritic ODS steels have been extensively characterized [21–23] at elevated temperatures. Dong et al. [22] measured the yield stress (YS) of mechanically alloyed and HIPed 16Cr-3Al ODS and reported the values of 750 MPa, 269 MPa, and 80 MPa at room temperature (RT), 600 °C and 800 °C, respec-

* Corresponding author at: School of Mechanical, Industrial and Manufacturing Engineering, Oregon State University, Corvallis, OR, 97330, United States.
E-mail address: somayeh.pasebani@oregonstate.edu (S. Pasebani).

https://doi.org/10.1016/j.jmst.2020.12.033
1005-0302/

tively. Mechanically alloyed and HIPed Fe-14Cr-2W-0.3Ti-0.3Y_2O_3 reduced activation ferritic (RAF) ODS showed YS values of 1280 MPa and 350 MPa at RT and 750 °C, respectively [23]. Mao et al. [24] evaluated thermal stability of the oxide particles in the Fe-12Cr-1.1W-0.2V-0.24Y-0.14Ta ODS steel and reported a high number density of $YTaO_4$ particles with a mean size of ~9 nm after MA and HIP with a significant coarsening up to 22 nm after 500 h at 1250 °C. Cunningham et al. [25] manufactured a nanostructured ferritic MA957 alloy via MA and HIP and investigated thermal aging up to 32,000 h at a temperature ranging from 800–1000 °C. The microstructure of MA957 was stable at T < 900 °C with slow but systematic coarsening at 950 °C, and especially at 1000 °C, accompanied by a slight reduction in the tensile strength [25].

Austenitic ODS alloys show a higher corrosion/oxidation resistance and a higher creep resistance at elevated temperatures than ferritic ODS alloys. However, only limited studies have been published on the high-temperature mechanical properties and thermal stability of austenitic ODS alloys [26]. For example, MA and HIPed 304 L+0.7 wt.% Zr alloy had an ultimate tensile strength (UTS) of 872 MPa at RT and 540 MPa at 500 °C. The elongation was measured to be 28.1 % at RT and 9.5 % at 500 °C [27]. According to Wang et al. [28], UTS values of 940 MPa and 415 MPa were reported for HIPed 304 ODS alloy at RT and 700 °C, respectively. Because 304L ODS alloy demonstrated enhanced mechanical properties at high temperatures compared to other austenitic ODS steels such as 316 L [26–30], the 304L ODS alloy has been selected as the focus of this study.

Boegelein et al. [31] utilized the LPBF process to fabricate thin-walled builds, using MA ODS-PM2000 (FeCrAl) powder. The YS of manufactured walls (330 MPa) was inferior to the conventionally produced PM2000 alloy (YS = 500 MPa). However, the YS could be enhanced further (to 450 MPa) by heat treatment due to the presence of atomic Y in the matrix and precipitation of fine Y-enriched particles. Walker et al. [32] demonstrated LPBF PM2000 ODS had larger-sized yttria-alumina oxides (54–61 nm) and an average particle size of 48 nm at laser scan speed of 100 mm/s and scan speed of 200 mm/s, respectively. Shi et al. [33] investigated the size, composition, and density of nanoparticles in Fe-9Cr-ODS alloy manufactured via laser engineered net shaping (LENS) and reported that the $Y_2Ti_2O_7$ and Y_2TiO_5 oxides formed during the LENS process, had similar compositions to the nanoparticles in the ODS steels produced with conventional powder metallurgy.

Conventional manufacturing of ODS alloys involves complex, expensive, and time-consuming MA resulting in contamination and inhomogeneous distribution of nanoparticles within the matrix [30]. A novel approach for the manufacturing of ODS alloys was introduced in our prior studies [34–38] in which the need for long hours of MA was eliminated. Instead, 304L ODS alloy was manufactured via LPBF process, allowing near-net-shape manufacturing without the need for hot consolidation and post-processing and machining. In RT, the LPBF 304L ODS alloy exhibited superior tensile properties (YS = 575 MPa) compared to wrought 304L (YS = 170 MPa) [39] and improved YS compared to LPBF 304L (YS = 540 MPa) [40]. The elongation of LPBF 304L ODS alloy was ~32 % [34], 4 % lower than LPBF 304L (36 %) [40], however, in comparison with other conventionally manufactured 304 ODS alloys (19 %–28 % at RT) [28,30], demonstrated higher elongation. The microstructure evolution and mechanical properties of LPBF 304L ODS alloy at RT have been investigated in detail in our previous work [34]. Therefore, the objective of this work is to examine high-temperature mechanical properties and creep resistance of LPBF 304L ODS alloy manufactured in our previous work [34]. Furthermore, the thermal stability of the LPBF 304L ODS alloy is evaluated. There is a gap in the literature on the thermal stability of austenitic ODS alloys whether conventionally and/or additively manufactured. Thus, the novelty of this work is to study the thermal stability of austenitic ODS alloys additively manufactured via LPBF process.

Table 1
The chemical composition of 304L powder according to Sandvik's datasheet (wt.%).

Fe	Ni	Cr	C	Si	Mn	P	S	N
Bal	10.060	18.853	0.017	0.720	1.3	0.012	0.005	0.083

2. Experimental

2.1. Sample production

Gas atomized spherical 304L stainless steel (median particle size, D_{50} = 33.3 μm) powder procured from Sandvik with chemical composition listed in Table 1 was mixed with 0.5 wt.% of yttrium oxide (purity of 99.99 %) with D_{50} = 0.968 μm from H.C. Starck in a planetary ball mill Retsch, PM100 for 4 h. The mixed powder of 304 L+0.5 wt.% yttrium oxide with D_{50} = 32.4 μm was used as feedstock for producing LPBF 304L ODS alloy samples.

Tensile bars and rectangular coupons were manufactured using an OR Creator LPBF machine equipped with a continuous wave Yb: YAG fiber laser (wavelength of 1067 nm) and a stainless steel build plate. Laser melting was performed in a nitrogen atmosphere, keeping the oxygen level in the build chamber <100 ppm to minimize oxidation. The LPBF parameters were optimized to obtain a relative density of >99 % by using the following process parameters: laser power of 145 W, the scan speed of 300 mm/s, the spot size of 50 μm, hatch spacing of 50 μm, and powder layer thickness of 30 μm. Further details about the feedstock preparation and LPBF process can be found elsewhere [34]. The density of the LPBF 304L ODS alloy samples was measured with the Archimedes method and was >99 %.

2.2. Thermal stability aging treatment

As-built specimens and a piece of pure Zr, as an oxygen getter, were sealed in evacuated quartz tubes filled with 99.999 % Ar as shown in Fig. 1(a). Then, the quartz tubes were placed in a Carbolite RHF box furnace and held for 100 h at temperatures of 1000, 1100, and 1200 °C. The temperature rapidly ramped up to 500 °C and reached the set temperature with 2.5 °C/min. The cooling rate was also 2.5 °C/min to 500 °C followed by furnace cooling.

2.3. Microstructure characterization

The phase identification in the samples was performed using X-ray diffraction (XRD, Bruker AXS D8 Discover) with Cu K_α target, operated at 40 kV and 40 mA. The microstructure of the samples was investigated by scanning electron microscopy (FEI Quanta 3D SEM). Before SEM characterization, a solution of 10 wt.% oxalic acid and 90 wt.% deionized water was used to electroetch LPBF 304L ODS samples by applying 15 V DC for 15 s. Samples for electron backscattered diffraction (EBSD) was polished in a vibratory polisher for 8 h using a 50 nm diamond slurry. The EBSD data collection was conducted by using an Orientation Imaging Microscopy (OIM) Data Collection 7.2 software in FEI Quanta 3D operating at 15 kV accelerating voltage, 1.7 nA beam current, and a step size of 500 nm.

An FEI TITAN 80–200 transmission electron microscope (TEM) equipped with ChemiSTEM technology was used to investigate the thermal stability of oxide nanoparticles and dislocation/nanoparticle interaction. The TEM samples were prepared, first by thinning down mechanically to a thickness of about 50–100 μm, and then 3-mm diameter disks were punched out of the samples. These disks were then electropolished using a twin-jet electropolisher (Fischione-110), operated at 15 V, and a tempera-

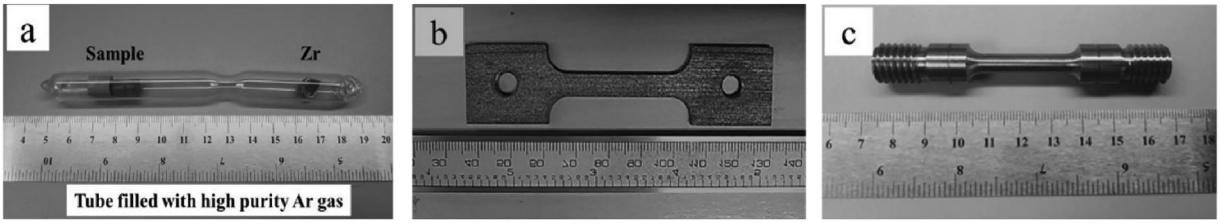

Fig. 1. (a) Evacuated quartz tube with LPBF 304L ODS sample and Zr (as oxygen getter) for thermal stability aging treatment, (b) high-temperature tensile specimens, and (c) cylindrical creep specimens were machined out of manufactured blocks.

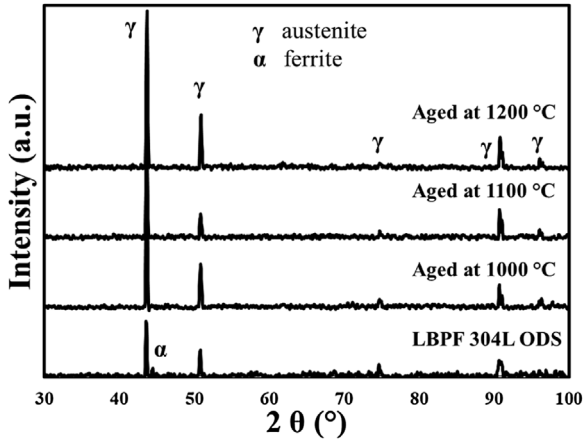

Fig. 2. XRD patterns of as-built LPBF 304 ODS alloy and aged at 1000, 1100, and 1200 °C.

ture of −10 °C in an electrolyte solution of 75 vol.% methanol and 25 vol.% HNO_3.

2.4. Mechanical properties and microhardness

A Leco microhardness tester (M-400A) at a load of 500 g was used to measure the hardness of LPBF 304L ODS samples; the mean of 10 indentations from cross-sections perpendicular to the build direction was reported. For various testing temperatures, sets of three dog bones, as presented in Fig. 1(b), were machined using wire electrical discharge machining (EDM) from rectangular blocks according to ASTM E8 (gauge width =6 mm, thickness =2 mm, gauge length =32 mm). The direction of testing dog bones was perpendicular to the build direction. Tensile tests were performed at a strain rate of 10^{-4} s^{-1}, at RT and high temperatures on the Instron 5969 machine equipped with an Instron furnace with a soaking time of 10 min.

Cylindrical creep specimens with a gauge length of 25.4 mm and a diameter of 6.53 mm were machined out of the LPBF-manufactured bars, as shown in Fig. 1(c). Three uniaxial constant-load creep tests in an Applied Test Systems 2335 lever arm (20:1 ratio) creep tester. The direction of the creep test was perpendicular to the build direction of specimens too. The creep tests were performed in air at 700 ± 1 °C under applied nominal stresses of 70, 85, and 100 MPa. Two Heidenhain ST-12 linear encoders measured the gauge elongation with an accuracy of ± 0.2 μm.

3. Results and discussion

3.1. Phase identification

The XRD patterns from the as-built LPBF 304L ODS alloy sample and the aged samples are presented in Fig. 2. The as-built sample showed the austenitic phase with a small trace of retained δ-ferrite phase due to rapid cooling [40]. However, after the aging treatment of LPBF 304L ODS samples at different temperatures, the remaining unstable δ-ferrite transformed into austenite phase. No other phases were detected in the XRD pattern of aged samples at all the temperatures, which suggests no secondary phase was formed after the aging process.

3.2. Effect of aging temperature on the microstructure of LPBF 304L ODS alloy

Fig. 3(a and b) shows the SEM micrograph from the cross-section perpendicular to the build direction of LPBF 304L ODS alloy in as-built and aged (at 1200 °C for 100 h) conditions, respectively. The typical cellular substructure in LPBF manufactured parts, which forms due to rapid solidification [41], was observed on the surface of the as-built LPBF 304L ODS alloy and shown in Fig. 3(a). Furthermore, the bright contrast nanoparticles that were homogeneously distributed within the matrix were observed in Fig. 3(a).

Fig. 3(b) shows a partial dissolution of cellular substructure in LPBF 304L ODS after aging at 1200 °C for 100 h. However, the cellular substructure was predominant indicating that the nanoparticles could stabilize the microstructure at 1200 °C. In our previous study on LPBF 304L stainless steel (with no yttria) [40], recrystallization occurred after annealing LPBF 304L for 2 h at 1200 °C, new grains with annealing twins formed in the 304L matrix, and the cellular microstructure completely disappeared. However, the cellular substructure remained partially unchanged in LPBF 304L ODS alloy after 100 h of aging at 1200 °C because of the promising thermal stability of the LPBF 304L ODS alloy due to presence of oxide nanoparticles [42].

The STEM high angle annular dark-field (HAADF) micrograph and corresponding EDS elemental maps of LPBF 304L ODS alloy before and after aging at 1200 °C for 100 h are shown in Fig. 4(a) and (b), respectively. There was a small porosity within the matrix as marked in the STEM HAADF micrograph of Fig. 4. Precipitation of spherical nanoparticles, as formerly shown in Fig. 3, are shown with white arrows in STEM HAADF micrograph of Fig. 4. Due to the high density of dislocation, especially in the as-built sample, inducing extra bright contrast in STEM HAADF micrograph, the detection of smaller nanoparticles was limited. However, the Y elemental map demonstrated a better contrast of formed nanoparticles in as-built and aged samples of LPBF 304L ODS alloy in Fig. 4. The compositional mapping in as-built LPBF 304L ODS alloy demonstrated micro-segregation at cell boundaries, leaving cell boundaries depleted from Fe, enriched in Cr, Si, Ni, and Mn.

In contrast to the initially added yttrium oxide (Y_2O_3) particles into the 304L feedstock, after the LPBF process, the precipitated nanoparticles within the 304L matrix were enriched in yttrium, silicon, and oxygen (Y-Si-O-enriched nanoparticles), as evident in Fig. 4(a). According to Ghayoor et al. [34] the morphology, size, and composition of these particles were transformed after LPBF process, conveying that the initial yttrium oxide particles in the feedstock were partially melted and supersaturated melt pool with Y and

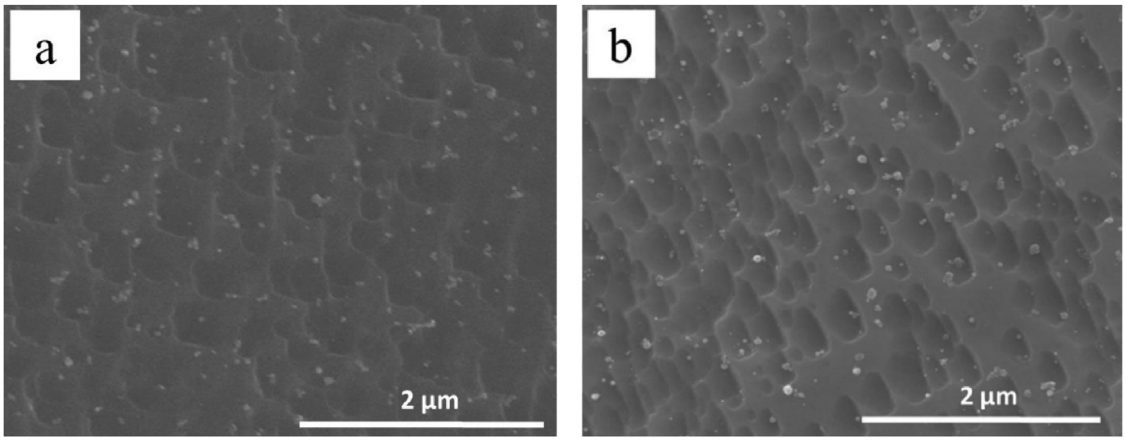

Fig. 3. SEM micrographs from the cross-section perpendicular to the build direction of (a) as-built LPBF 304L ODS alloy and (b) aged LPBF 304L ODS at 1200 °C for 100 h.

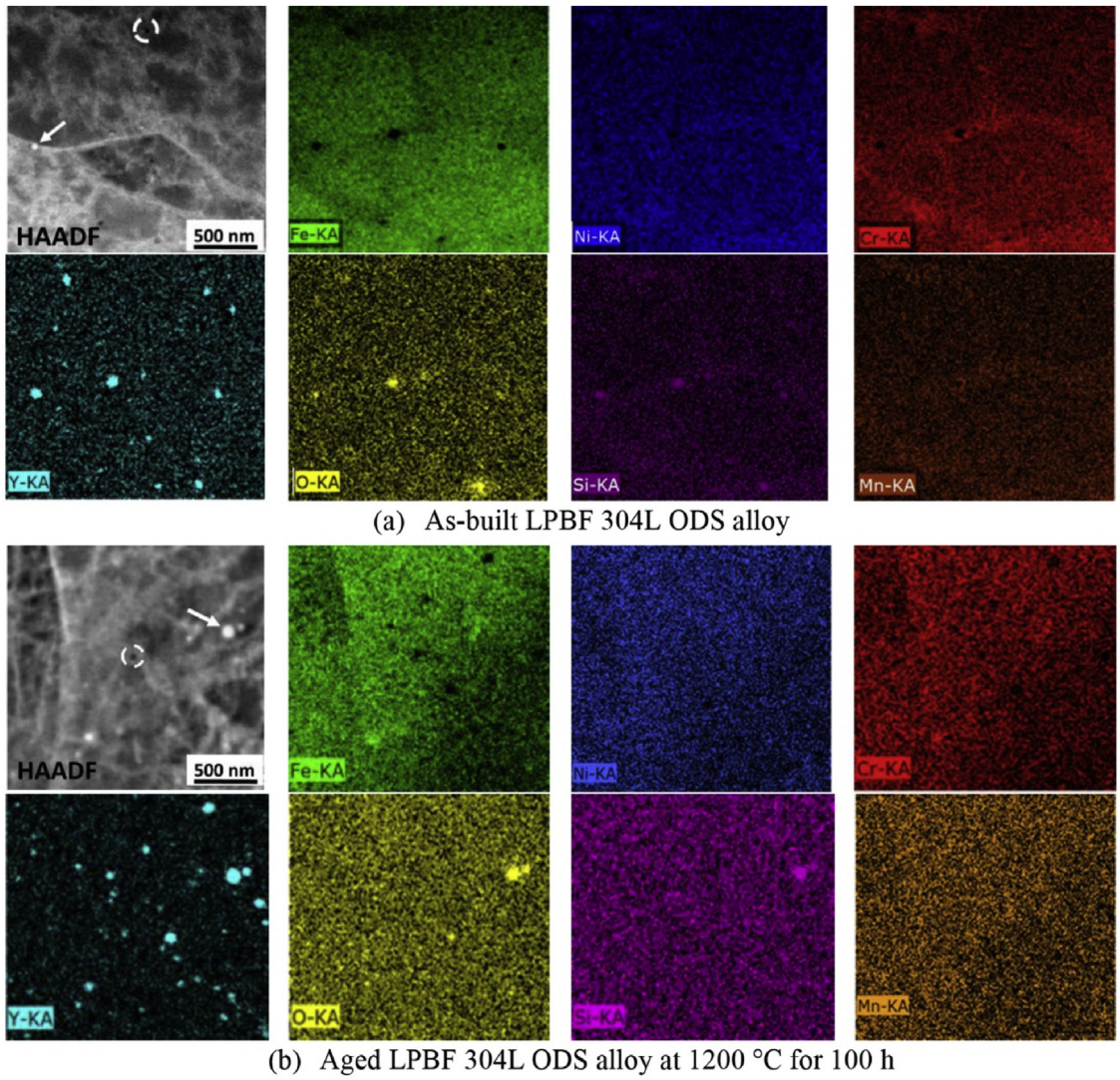

Fig. 4. HAADF (Z-contrast) STEM micrograph with corresponding EDS elemental maps (arrows point at Y-Si-O-enriched nanoparticles, and dashed circles present pores in the matrix) in (a) as-built LPBF 304L ODS alloy, and (b) aged LPBF 304L ODS alloy at 1200 °C for 100 h.

O atoms. Two different phenomena were proposed for partially melting of yttrium oxide particles as follow: (1) The high intensity of laser beam combined with the high surface-to-volume ratio of yttrium oxide nanoparticles; (2) a substantial decrease in the melting point of yttrium oxide due to loss of oxygen atoms from the crystal structure of yttrium oxide at high temperatures [34]. Due to the immiscibility of iron and yttrium [43], it can be expected the Y and O atoms reacted with the available Si atoms from the

Table 2
EDS chemical analysis of precipitated nanoparticles enriched in Y-Si-O (wt.%).

Elements	Fe	Cr	Ni	Mn	Si	Y	O
Nanoparticles of as-built LPBF 304L ODS alloy (wt.%)	41.27 ± 8.2	13.59 ± 3.4	6.47 ± 1.5	1.59 ± 0.1	2.59 ± 0.4	12.77 ± 2.4	21.73 ± 5.2
Nanoparticles of aged LPBF 304L ODS alloy at 1200 °C for 100 h (wt.%)	56.69 ± 6.3	16.54 ± 2.6	7.3 ± 2.2	1.17 ± 0.2	0.18 ± 0.03	17.32 ± 2.9	0.79 ± 0.08

304L matrix and upon solidification, the yttrium-silicate (Y-Si-O) nanoparticles precipitated within the matrix. Further detail about the formation mechanism of yttrium-silicate nanoparticles can be found elsewhere [34,35].

The micro-segregation of elements at cell boundaries disappeared due to the accelerated diffusion of elements upon aging at high temperatures as shown in Fig. 4(b). Furthermore, the corresponding EDS map demonstrated that the yttrium-silicate nanoparticles were still stable at the high temperature of 1200 °C after 100 h of aging, despite a slight variation in the chemical composition. The point EDS analysis on nanoparticles before and after aging exhibited the nanoparticles gained Y atoms during the aging process. This comparison is given in Table 2. In ODS alloys, the diffusion of the yttrium element is reported as one of the main reasons for the growth of nanoparticles through the Ostwald ripening mechanism. During the aging process, Y atoms migrate to form coarser particles with reduced surface tension [44]. Furthermore, Ribis et al. [45] have confirmed that the coarsening of Y-rich nanoparticles was related to the growth kinetics of yttrium diffusion. The growth of nanoparticles during aging will be discussed further in the following paragraphs. Moreover, the EDS point analysis revealed that the amount of oxygen in nanoparticles drastically decreased after aging. Similar behavior on the drop of the oxygen content of nanoparticles is reported in the aging of conventionally manufactured ODS alloys [24,25].

The in-depth microstructure of the as-built LPBF 304L ODS and aged at 1200 °C are shown in Fig. 5. A hexagon cellular substructure with cell size <500 nm and high dislocation density, was observed in the as-built specimen as shown in Fig. 5(a) and (c). Using different STEM micrographs and adopting the line-intercept method, the dislocation density was estimated to be $\sim(2.11 \pm 0.2) \times 10^{14}$ (m^{-2}) in the as-built sample. It was difficult to observe nanoparticles at higher magnification shown in Fig. 5(c) because the high density of dislocations masked the presence of Y-Si-O nanoparticles. The high cooling rate of LPBF process generated thermal stresses, leading to the creation of a high density of dislocations within the matrix [41]. Furthermore, a trace of cellular substructure was detected in the microstructure of the aged sample as shown in Fig. 5(b) and (d). The cell walls in the aged sample were decorated with a lower dislocation density (measured to be $\sim(1.68 \pm 0.14) \times 10^{14}\ m^{-2}$) due to recovery. Remaining dislocations imply the promising thermal stability of LPBF 304L ODS alloy due to the presence of thermally stable oxide nanoparticles preventing full recrystallization and further grain growth after 100 h of aging treatment at 1200 °C.

At least 500 oxide nanoparticles were selected from random regions in different samples using several SEM and STEM micrographs to illustrate the oxide nanoparticle size histogram shown in Fig. 6. The histogram indicates that the nanoparticles size ranged 15–75 nm. Initially, the spherical nanoparticles with the mean size of 25 ± 10 nm were homogeneously distributed within the as-built LPBF 304L ODS matrix as shown in Fig. 6(a). After aging for 100 h at different temperatures of 1000, 1100, and 1200 °C the mean size of nanoparticles was measured to be 36 ± 13 nm, 38 ± 13 nm, and 50 ± 15 nm, respectively and are shown in Fig. 6(b)-(d). The fraction of nanoparticles <20 nm decreased dramatically, plausibly due to the nanoparticles coarsening under the Ostwald ripening mechanism. Smaller particles dissolved to reduce the surface tension and the energy of the system, while the larger particles continuously grew during the thermal aging to reduce the area of particles/matrix interface [46].

Fig. 7 presents the EBSD inverse pole figures (IPF) map and the corresponding misorientation angle chart for the LPBF 304L ODS alloy before and after aging. Columnar grains in LPBF 304L ODS alloy did not display a preferred orientation, or texture, as shown in Fig. 7(a). Unlike our previous work on LPBF 304 L, in which the annealing twins formed after 2 h of annealing at 1200 °C [40], no evidence of recrystallization, twinning, and grain growth was detected in the IPF map of aged LBPF 304L ODS samples shown in Fig. 7(b)–(d).

Table 3 presents the grain sizes of the as-built and aged samples based on the results shown in Fig. 7(a)–(d). Despite a slight variation in the grain size of the as-built and aged samples, grain size did not significantly increase (<20 % at 1200 °C for 100 h), demonstrating a promising thermal stability of LPBF 304L ODS alloy at temperatures >1000 °C. Furthermore, the misorientation angle charts presented in Fig. 7(a)–(d), demonstrate the presence of a high fraction of low angle grains boundaries (LAGB) with misorientation of <10° in LPBF 304L ODS alloy before and after aging. Hence, the transformation from LAGB to high-angle grain boundaries (HAGB, >10°), known as recrystallization was effectively hindered due to Zener pinning [47].

3.3. Effect of high temperature on the mechanical properties

The YS, UTS, and elongation values of LPBF 304L ODS alloy tested at various temperatures are presented in Fig. 8 and summarized in Table 4. At RT, the value of YS and UTS of LPBF 304L ODS alloy were 575 ± 8 MPa and 700 ± 13 MPa, respectively. These high tensile properties at RT were attributed to the combined effects of very small grain size, high density of dislocations, and oxide nanoparticles [34].

By increasing temperature from RT to 800 °C, a decreasing trend in tensile properties of LPBF 304L ODS alloy was observed as shown in Fig. 8(a). The YS and UTS values at 400 °C, dropped to 345 ± 6 MPa and 411 ± 1 MPa, respectively, which were considerably lower than the same properties at RT. By raising the temperature to 500 °C and 600 °C, the YS values slightly decreased to 319 ± 4 MPa and 290 ± 2 MPa, respectively. This phenomenon between 400–600 °C can be primarily attributed to the softening behavior resulting from the annihilation of dislocations, subsequent coarsening of the grains/subgrains as a result of recovery, and particle coarsening [48,49]. Beyond 600 °C, the YS of the LPBF 304L ODS alloy fell precipitously to 217 ± 1 MPa and 145 ± 5 MPa, at 700 °C and 800 °C, respectively. In general, the total elongation of LPBF 304L ODS alloy showed a similar trend to YS and UTS, as shown in Fig. 8(b). The elongation of LPBF 304L ODS alloy at RT was 32 %±5 % and dropped to 23.5 %±2 % at 400 °C. Eventually, the elongation slightly decreased to 23 %±1 % at 600 °C and then dropped to 18.5 %±1 % at 800 °C.

Table 5 compares the mechanical properties of LPBF 304L ODS with 304 annealed [39], HIP 310 ODS [50], HIP 304 ODS [28,30], HIP 316 ODS [51], HIP Fe16Cr3Al ODS [22], SPS Fe14Cr ODS [17] and PM2000 ODS [52]. At 600 °C, the LPBF 304L ODS alloy demonstrated YS of 290 MPa, whereas the YS of 304L annealed was 113 MPa at the same temperature. A remarkable discrepancy in the reported values for YS and UTS at different temperatures can be attributed

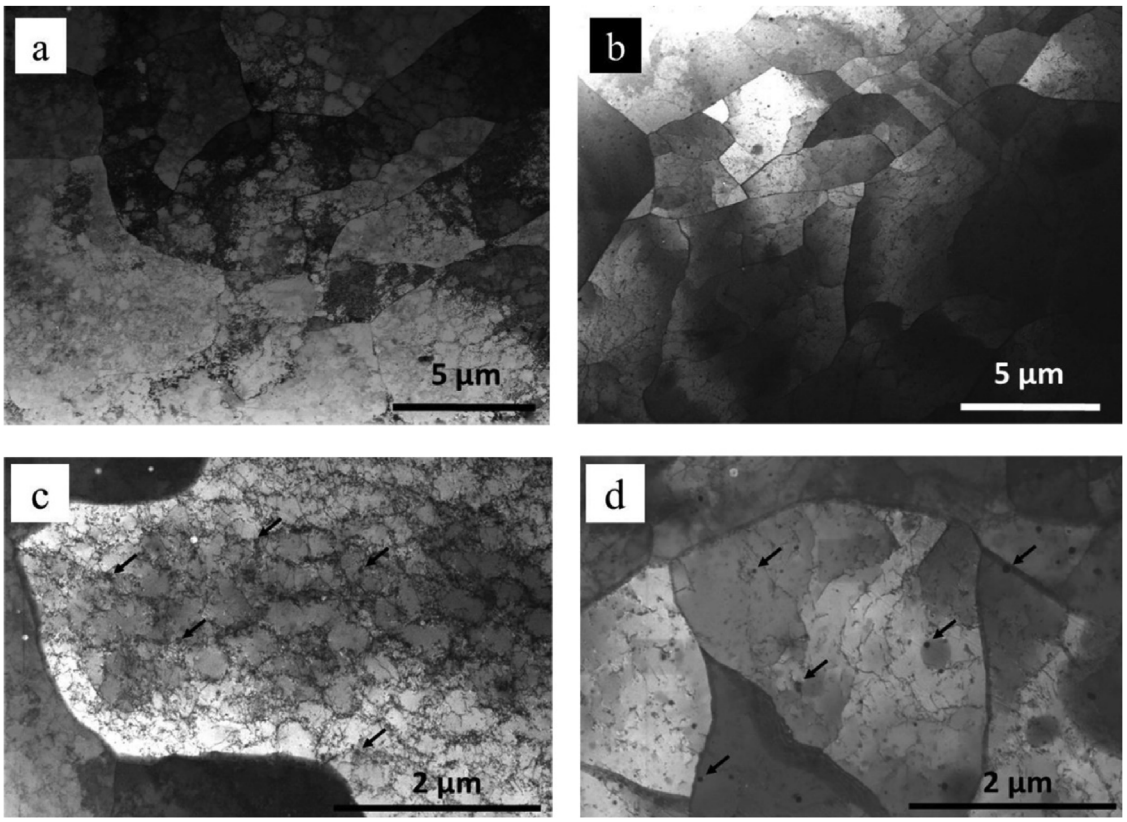

Fig. 5. Bright-field STEM micrographs (a), (c) as-built LPBF 304L ODS alloy (b), (d) aged LPBF 304L ODS alloy at 1200 °C for 100 h, arrows pointing at oxide nanoparticles.

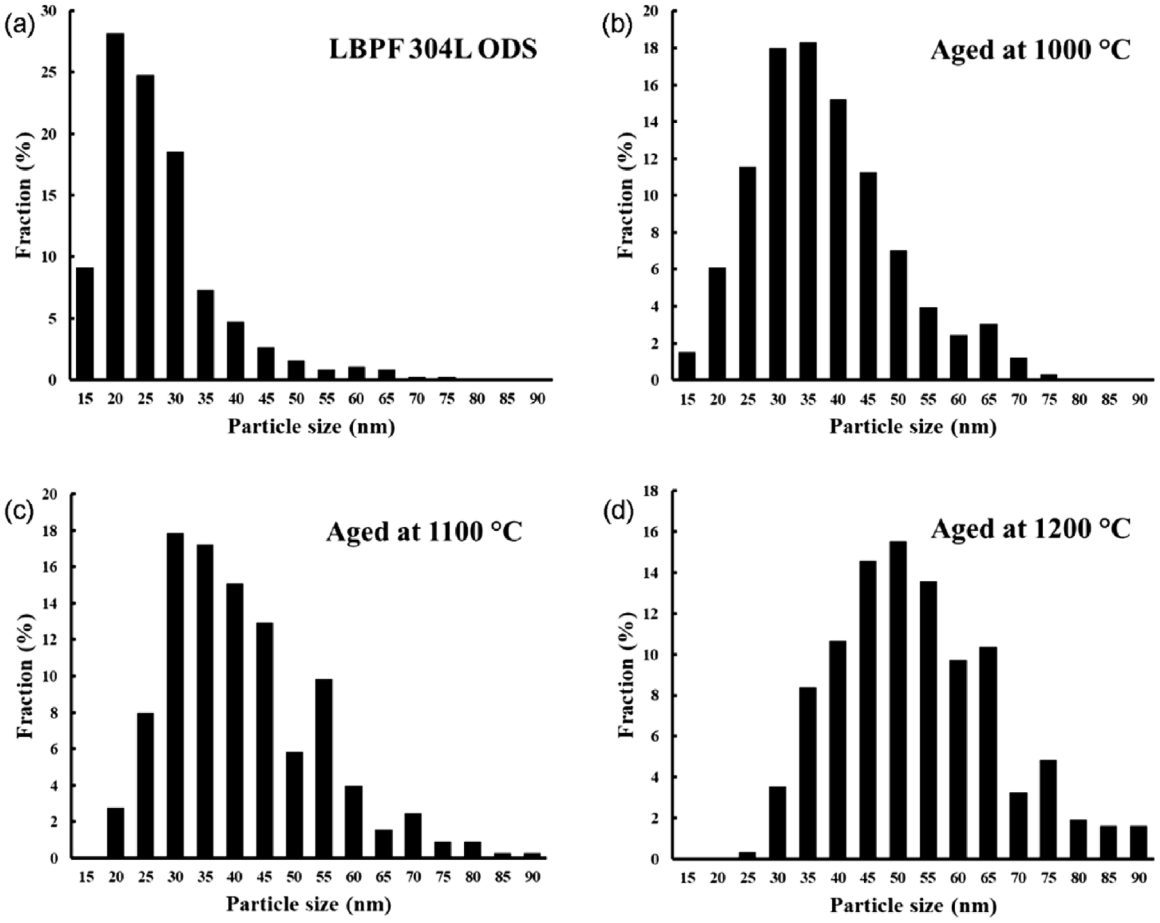

Fig. 6. Histogram of the oxide nanoparticle size distribution of LPBF 304L ODS alloy (a) as-built and after aging at (b) 1000 °C, (c) 1100 °C, and 1200 °C for 100 h.

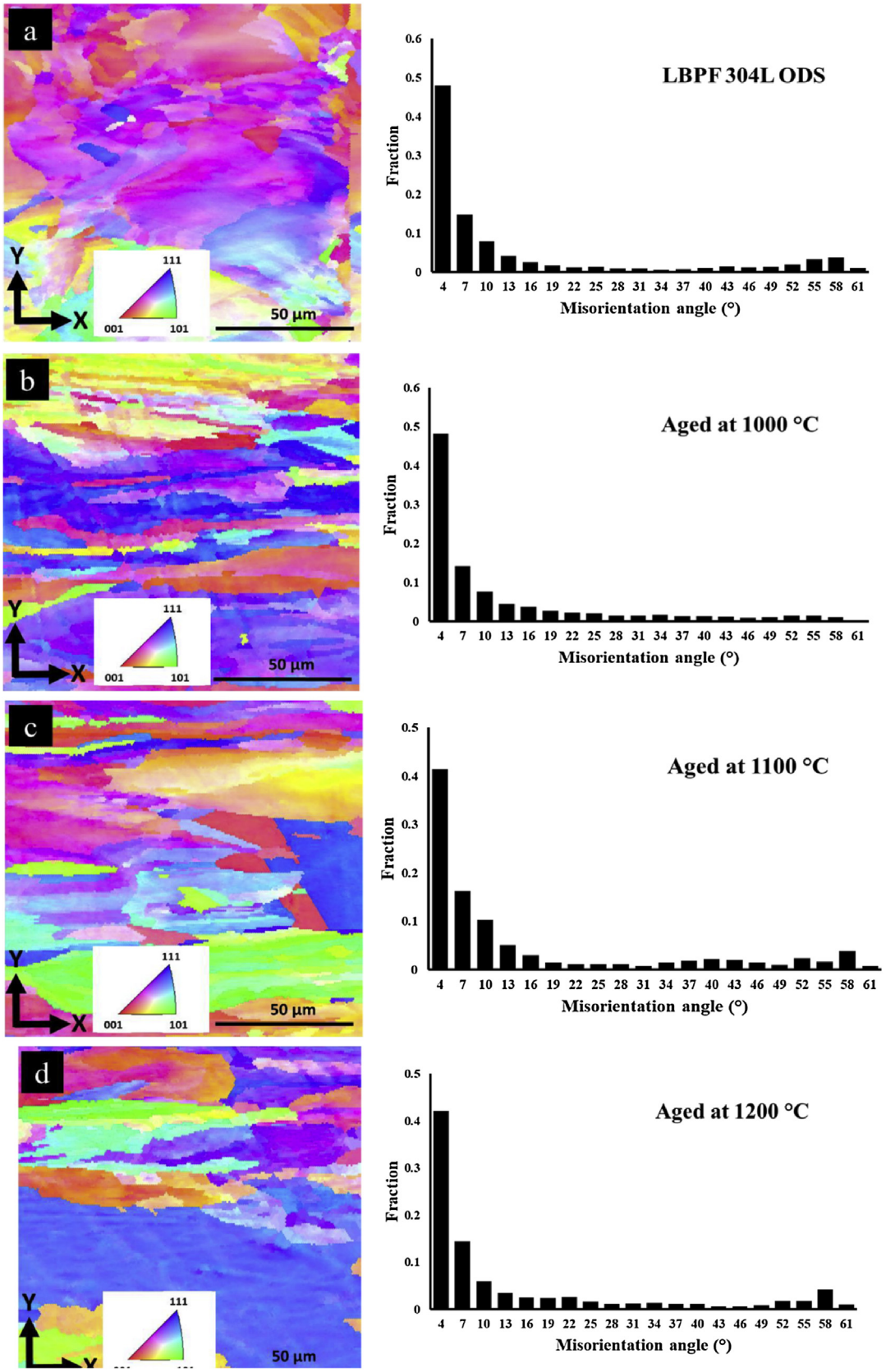

Fig. 7. IPF maps and corresponding grain misorientation angle in LPBF 304L ODS alloy (a) as-built and after aging at (b) 1000 °C, (c) 1100 °C and (d) 1200 °C for 100 h; grain tolerance angle was set at 5° and misorientation angle above 10° considered to be high angle grain boundaries (HAGB).

Table 3
Grain size measurement in LPBF 304L ODS as-built, and aged at 1000, 1100, and 1200 °C using EBSD micrographs shown in Fig. 7(a)-(d).

Samples	As-built	Aged at 1000 °C	Aged at 1100 °C	Aged at 1200 °C
Average grain size (μm)	7.7 ± 6.7	8.3 ± 6.1	8.2 ± 5.8	9.1 ± 7.2

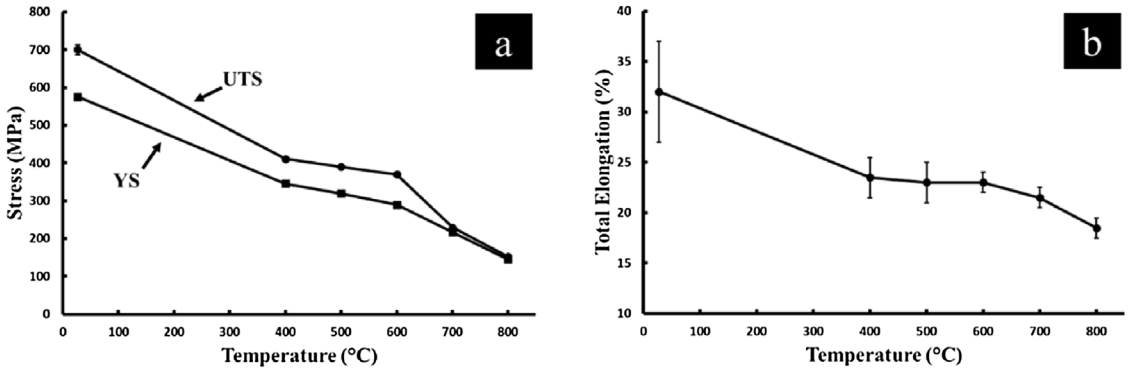

Fig. 8. High-temperature tensile properties of the LPBF 304L ODS alloy at different temperatures: (a) YS and UTS values, and (b) total percentage elongation to fracture.

Table 4
Tensile properties of LPBF 304L ODS alloy at room temperature, 400 °C, 500 °C, 600 °C, 700 °C and 800 °C.

Tensile properties	RT	400 °C	500 °C	600 °C	700 °C	800 °C
YS (MPa)	575 ± 8	345 ± 6	319 ± 4	290 ± 2	217 ± 1	145 ± 5
UTS (MPa)	700 ± 13	411 ± 1	390 ± 2	370 ± 4	229 ± 1	152 ± 6
Elongation (%)	32 ± 5	23.5 ± 2	23 ± 2	23 ± 1	21.5 ± 1	18.5 ± 1

Table 5
A comparison of YS and UTS values of LPBF 304L ODS alloy with annealed 304 and conventionally manufactured austenitic and ferritic ODS alloys.

Material	YS at RT	UTS at RT	YS at 600 °C	UTS at 600 °C	YS at 700 °C	UTS at 700 °C	YS at 800 °C	UTS at 800 °C
LPBF 304L ODS (present study)	575	700	290	370	217	229	145	152
Annealed 304 [39]	290	579	113	367	95	241	68	124
HIP 310 ODS [50]	526	904	—	—	—	350	—	—
HIP 304 ODS [28]	525	940	—	—	—	415	—	—
HIP 304 ODS [30]	—	775	—	410	—	300	—	—
HIP 316 L ODS [51]	370	670	—	—	220	270	—	—
HIP Fe16Cr3Al ODS [22]	750	850	269	350	—	—	80	85
SPS Fe14Cr ODS [17]	620	760	300	350	220	300	—	—
PM2000 ODS [52]	850	880	420	450	—	—	180	200

to a large variation in the composition and processing of conventionally manufactured ferritic and austenitic ODS alloys. The LPBF 304L ODS alloy demonstrated a comparable YS value to other conventionally manufactured austenitic ODS alloys but an inferior YS to the conventionally manufactured ferritic ODS alloys at RT. At temperatures of 600 °C and 700 °C, the YS value of LPBF 304L ODS alloy was 290 MPa and 217 MPa, respectively which are similar to that of the ferritic Fe-Cr ODS alloys [17,22]. The UTS value of the LPBF 304L ODS alloy at 700 °C was about 100 MPa lower than that of other conventionally manufactured austenitic ODS alloys [28,50].

The variation in microhardness values as a function of the aging temperature is shown in Fig. 9. In the as-built LPBF 304L ODS alloy, the microhardness was 350 ± 12 HV which is substantially higher than LPBF 304L (235 ± 3 HV) [40] and conventionally manufactured austenitic ODS alloys, ranged 240–300 HV [50,53]. The high hardness of LPBF 304L ODS alloy was attributed to the homogeneous distribution of nanoparticles; enhancing the mechanical properties through dispersion hardening mechanism (Orowan) [54]. After the aging of samples at 1000 °C for 100 h, the microhardness dropped significantly from 350 ± 12 HV to 180 ± 15 HV. This microhardness drop can be attributed to the recovery and annihilation of dislocations after aging, and coarsening of nanoparticles at high-temperature aging as shown in Figs. 5 and 6. Aged samples at higher temperatures of 1100 °C and 1200 °C showed hardness of 181 ± 12 HV and 181 ± 13 HV, respectively, indicating no further recovery [49].

3.4. Creep test at 700 °C

Fig. 10 shows the creep curves of LPBF 304L ODS alloy at a temperature of 700 °C under three different (initial) applied stresses of 70, 85, and 100 MPa. The selection of 700 °C as our test temperature was based on the available studies on the creep properties of 304 stainless steel and our creep tester temperature limit. At 700 °C, all the creep curves exhibit a relatively short period of primary creep as compared with the other stages of creep. This shows that the strain hardening effect was recovered soon after the load was applied. The tertiary stage where the slope of the creep curve (i.e. creep rate) increased continuously until rupture lasted the longest time as shown in Fig. 10. Under the lowest stress of 70 MPa, the specimen crept >1400 h, before the creep rupture occurred. However, with the increase in applied stress, the rupture life decreased correspondingly. Table 6 summarizes the rupture time as a function of the applied stresses.

The minimum strain rate for each creep curve was determined from Fig. 10 and plotted as a function of applied stress as shown in Fig. 11(a). The following Norton's power law [55] was

Table 6
Creep-rupture times under applied stress of 70, 85, and 100 MPa at 700 °C.

Stress (MPa)	Rupture Time (h)
70	1,471.3
85	577.5
100	153.2

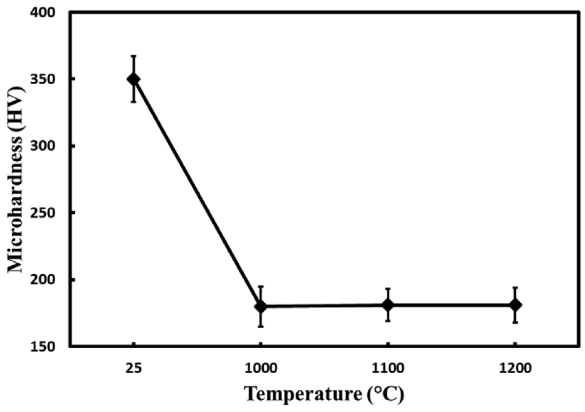

Fig. 9. Microhardness values of LPBF 304L ODS alloy before and after aging for 100 h.

used to correlate the minimum strain rate with applied stress at 700 °C:

$$\dot{\varepsilon}_{\min} = A\sigma^n \quad (1)$$

where $\dot{\varepsilon}_{\min}$ is the minimum creep rate, A is temperature-dependent material constant, σ is the applied stress, and n is the stress exponent. The slope of the fitted straight line plot gave the relevant stress exponent (n). A stress exponent of ~7.7 was determined from the plot shown in Fig. 11(a). Furthermore, 700 °C creep data from a conventional 304 SS are included for comparison on the same plot in Fig. 11 [56]. The creep rates of LPBF 304L ODS alloy were about two orders of magnitude lower than 304 SS. At a higher stress range, the conventional 304 SS exhibits a creep stress exponent of ~7.0 and toward the lower stress range, a transition seems albeit not very clear due to the lack of further low-stress data [56]. A value of n in the range of 3–8 represents a dislocation type of creep mechanism [57]. In the current study, from the stress exponent values of both conventional 304 SS (n = 7) and LBPF 304L ODS (n = 7.7) at T = 700 °C, the micromechanisms appear to be related to a climb-related dislocation creep mechanism [57].

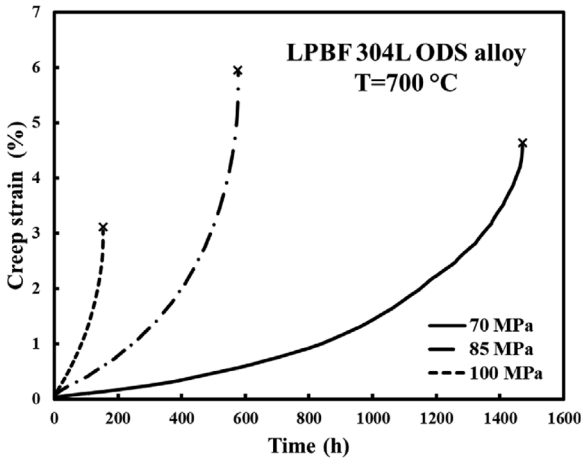

Fig. 10. Creep curves of LPBF 304L ODS alloy for applied stress of 70, 85, and 100 MPa at 700 °C.

The minimum creep rate and the rupture life depends on the normalized creep stress by the yield stress; therefore, using an alternative empirical approach, creep data could be plotted using the normalized applied creep stress as shown in Fig. 11(b). From the data presented in Fig. 11(b), the normalized creep stress and the minimum creep rate of LPBF 304L ODS alloy at 100 MPa were 0.46 and 2.44×10^{-8} s^{-1}, respectively. In comparison, at the same applied stress, the same creep parameters of conventional 304 SS were 1.05 and 5×10^{-6} s^{-1} [58], respectively. The normalized creep stress could explain the large difference in the minimum creep rate of conventionally 304 SS and LPBF 304L ODS alloy. Intrinsically, the LPBF 304L ODS alloy was stronger than conventional 304 SS, and hence while the difference in yield stress is taken into account, the two plots, Fig. 11(a) and (b), lined up well. Further specific identification of the rate-controlling creep mechanism was not feasible at this time as more creep data are needed to fully analyze the creep data. A more detailed investigation should be adopted to fully understand the creep behavior of LPBF 304L ODS alloy. However, according to Figs. 10 and 11, the present study demonstrated that the presence of Y–Si–O nanoparticles effectively hindered dislocation movement and led to an enhancement of creep resistance at 700 °C.

4. Conclusions

In summary, the thermal stability of oxide nanoparticles of additively manufactured austenitic 304L ODS alloy at high-temperature

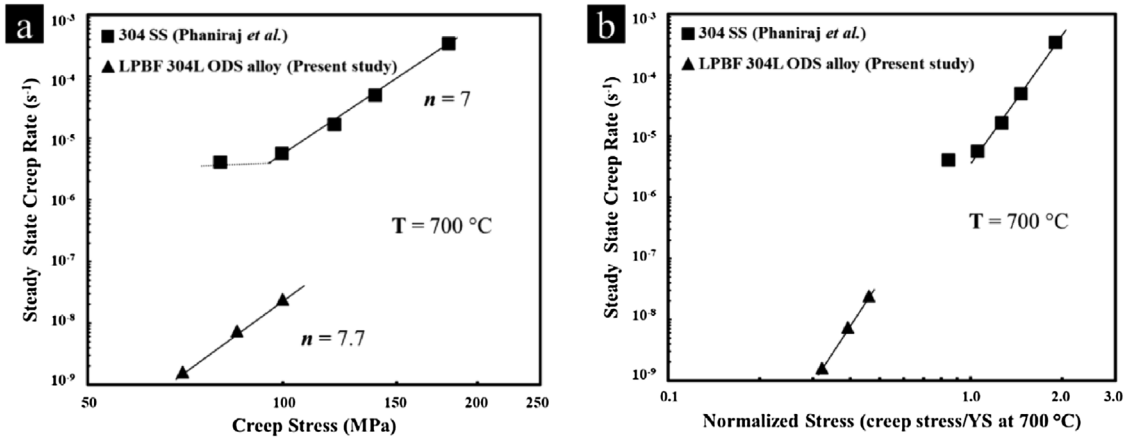

Fig. 11. The variation of (a) steady-state creep rate versus stress at 700 °C as double logarithmic plots and (b) steady-state creep rate versus normalized stress (creep stress/YS at 700 °C) for LPBF 304L ODS alloy (present study) and comparison with 304 SS creep data taken from the work of Phaniraj et al. [56].

aging treatment (1000, 1100, and 1200 °C for 100 h) was investigated in detail. Furthermore, the high-temperature (400–800 °C) mechanical properties and creep resistance of LPBF 304L ODS alloy were evaluated. The key results and findings can be summarized as follows:

(1) The as-built LPBF 304L ODS alloy exhibited a cellular substructure with a high density of dislocations ($2.11 \pm 0.2 \times 10^{14}$ m^{-2}). Aging the LPBF 304L ODS alloy at 1200 °C for 100 h did not significantly alter the microstructure. The cellular substructure could be detected, however, the density of dislocation dropped to $1.68 \pm 0.14 \times 10^{14}$ m^{-2} due to annihilation and recovery.
(2) The nanoparticles with an average size of 25 ± 10 nm were homogeneously distributed within the 304L matrix. Nanoparticles coarsened to 50 ± 15 nm after holding 100 h at 1200 °C due to the Oswald ripening mechanism.
(3) EBSD analysis revealed that after 100 h of aging the LPBF 304L ODS alloy at 1200 °C, the LBPF 304L ODS sample still had a significant fraction of LAGB, confirming that the nanoparticles controlled the recrystallization stage and retarded further grain growth.
(4) The LPBF 304L ODS alloy displayed comparable tensile properties at high temperatures with conventionally manufactured austenitic and ferritic ODS alloys. At 600 °C and 800 °C, the YS was 290 MPa and 145 MPa, respectively, substantially higher than 304 in the annealed condition with values of 113 MPa, and 68 MPa, respectively.
(5) The creep properties of LPBF 304L ODS alloy were investigated at a temperature of 700 °C under applied stress of 70, 85, and 100 MPa. The stress exponent (n) of LPBF 304L ODS alloy was determined to be ~7.7, and creep rates were found to be about two orders of magnitude lower than for conventionally manufactured 304 stainless steel under an equivalent stress level.

Declaration of Competing Interest

The authors declare that they have no known competing financial interests or personal relationships that could have appeared to influence the work reported in this paper.

Acknowledgments

The authors would like to thank Dr. Xu (principal investigator of Materials Modeling and Development Group), Dr. Tucker, principal investigator, and Dr. Rolly, lab manager of Nuclear Materials and Metallurgy Group at Oregon State University for helping with the thermal stability aging treatment. Also, the authors would like to acknowledge the funding of critical equipment provided by the Murdock Charitable Trust (No. 2016231:MNL:5/18/2017), the RAPID Institute, the U.S. DOE (No. DE-EE0007888), and the NSF Advanced Manufacturing Program (No. 1856412) for the financial support. The authors also thank the OSU electron microscopy center and ATAMI facility staff and director.

References

[1] K. Saeidi, X. Gao, Y. Zhong, Z.J. Shen, Mater. Sci. Eng. A 625 (2015) 221–229.
[2] S. Mirzababaei, S. Pasebani, J. Manuf. Mater. Proc. 3 (2019) 82.
[3] N. Travitzky, A. Bonet, B. Dermeik, T. Fey, I. Filbert-Demut, L. Schlier, T. Schlordt, P. Greil, Adv. Eng. Mater. 16 (2014) 729–754.
[4] M. Marandi, J. Tarbutton, Proc. Manuf. 34 (2019) 666–671.
[5] K.S. Baghbaderani, M. Nematollahi, P. Bayatimalayeri, H. Dabbaghi, A. Jahadakbar, M. Elahinia, arXiv preprint arXiv 2006 (2020) 15659.
[6] A.S. Raman, K.R. Haapala, K. Raoufi, B.S. Linke, W.Z. Bernstein, K.C. Morris, Smart Sustain. Manuf. Syst. 2 (2020) 1–24.
[7] S. Mirzababaei, B.K. Paul, S. Pasebani, JOM 72 (2020) 3070–3079.
[8] M. Katancik, S. Mirzababaei, M. Ghayoor, S. Pasebani,J. Alloys. Compd. 849 (2020), 156319.
[9] X. Li, C. Kang, H. Huang, L. Zhang, T.B. Sercombe, Mater. Sci. Eng. A 606 (2014) 370–379.
[10] M. Nematollahi, G. Toker, S. Saghaian, J. Salazar, M. Mahtabi, O. Benafan, H. Karaca, M. Elahinia, Shape Mem. Superelasticity 5 (2019) 113–124.
[11] S. Pasebani, M. Ghayoor, S. Badwe, H. Irrinki, S.V. Atre, Addit. Manufact. 22 (2018) 127–137.
[12] H. Dabbaghi, K. Safaei, M. Nematollahi, P. Bayati, M. Elahinia, Materials 13 (2020) 2104.
[13] M. Ghayoor, S.B. Badwe, H. Irrinki, S.V. Atre, S. Pasebani, Mater. Sci. Forum 941 (2018) 698–703.
[14] G.R. Odette, M.J. Alinger, B.D. Ann, Rev. Mater. Res. 38 (2008) 471–503.
[15] H. Oka, M. Watanabe, S. Ohnuki, N. Hashimoto, S. Yamashita, S. Ohtsuka, J. Nucl. Mater. 447 (2014) 248–253.
[16] Y. Miao, K. Mo, B. Cui, W.-Y. Chen, M.K. Miller, K.A. Powers, V. McCreary, D. Gross, J. Almer, I.M. Robertson, J.F. Stubbins, Mater. Charact. 101 (2015) 136–143.
[17] M.A. Auger, V. De Castro, T. Leguey, A. Muñoz, R. Pareja, J. Nucl. Mater. 436 (2013) 68–75.
[18] X. Yan, X. Zhang, F. Wang, T. Stockdale, Y. Dzenis, M. Nastasi, B. Cui, JOM 71 (2019) 2856–2867.
[19] G. Schaffer, M. Loretto, R. Smallman, J. Brooks, Acta Metall. 37 (1989) 2551–2558.
[20] P. Krautwasser, A. Czyrska-Filemonowicz, M. Widera, F. Carsughi, Mater. Sci. Eng. A 177 (1994) 199–208.
[21] S. Dryepondt, K.A. Unocic, D.T. Hoelzer, C.P. Massey, B.A. Pint, J. Nucl. Mater. 501 (2018) 59–71.
[22] H. Dong, L. Yu, Y. Liu, C. Liu, H. Li, J. Wu, Fusion Eng. Des. 125 (2017) 402–406.
[23] Z. Oksiuta, M. Lewandowska, K.J. Kurzydłowski, Mech. Mater. 67 (2013) 15–24.
[24] X. Mao, T.K. Kim, S.S. Kim, K.H. Oh, J. Jang, J. Nucl. Mater. 428 (2012) 82–89.
[25] N. Cunningham, Y. Wu, D. Klingensmith, G.R. Odette, Mater. Sci. Eng. A 613 (2014) 296–305.
[26] L. Raman, K. Gothandapani, B.S. Murty, Def. Sci. J. 66 (2016) 316–322.
[27] D. Morrall, J. Gao, Z. Zhang, K. Yabuuchi, A. Kimura, T. Ishizaki, Y. Maruno, Nucl. Mater. Energy 15 (2018) 92–96.
[28] M. Wang, Z. Zhou, H. Sun, H. Hu, S. Li, Mater. Sci. Eng. A 559 (2013) 287–292.
[29] Z. Zhou, S. Yang, W. Chen, L. Liao, Y. Xu, J. Nucl. Mater. 428 (2012) 31–34.
[30] Y. Xu, Z. Zhou, M. Li, P. He, J. Nucl. Mater. 417 (2011) 283–285.
[31] T. Boegelein, S.N. Dryepondt, A. Pandey, K. Dawson, G.J. Tatlock, Acta Mater. 87 (2015) 201–215.
[32] J.C. Walker, K.M. Berggreen, A.R. Jones, C.J. Sutcliffe, Adv. Eng. Mater. 11 (2009) 541–546.
[33] Y. Shi, Z. Lu, H. Xu, R. Xie, Y. Ren, G. Yang, J. Alloys. Compd. 791 (2019) 121–133.
[34] M. Ghayoor, K. Lee, Y. He, C.-H. Chang, B.K. Paul, S. Pasebani,Mater. Sci. Eng. A 788 (2020), 139532.
[35] M. Ghayoor, K. Lee, Y. He, C.-H. Chang, B.K. Paul, S. Pasebani, Microsc. Microanal. 25 (2019) 2594–2595.
[36] B.K. Paul, K. Lee, Y. He, M. Ghayoor, C.H. Chang, S. Pasebani, CIRP Annals 69 (2020) 193–196.
[37] M. Ghayoor, S. Mirzababaei, K. Lee, Y. He, C.-H. Chang, B.K. Paul, S. Pasebani, Proceedings of the 30th Annual International Solid Freeform Fabrication Symposium – an Additive Manufacturing Conference, Austin, TX, 2019, pp. 967–976.
[38] S. Mirzababaei, M. Ghayoor, R.P. Doyle, S. Pasebani,Mater. Lett. 284 (2021), 129046.
[39] A. Iron, S. Institute, High-temperature Characteristics of Stainless Steels, Committee of Stainless Steel Producers, American Iron and Steel Institute, 1979.
[40] M. Ghayoor, K. Lee, Y. He, C.H. Chang, B.K. Paul, S. Pasebani,Addit. Manuf. 32 (2020), 101011.
[41] Y.M. Wang, T. Voisin, J.T. McKeown, J. Ye, N.P. Calta, Z. Li, Z. Zeng, Y. Zhang, W. Chen, T.T. Roehling, R.T. Ott, M.K. Santala, P.J. Depond, M.J. Matthews, A.V. Hamza, T. Zhu, Nat. Mater. 17 (2018) 63–71.
[42] R. Magnabosco, Mater. Res. 12 (2009) 321–327.
[43] J. Nelson, D. Riley, Proc. Phys. Soc. Lond. (1945) 160–177.
[44] H. Sakasegawa, L. Chaffron, F. Legendre, L. Boulanger, T. Cozzika, M. Brocq, Y. de Carlan, J. Nucl. Mater. 384 (2009) 115–118.
[45] J. Ribis, Y. De Carlan, Acta Mater. 60 (2012) 238–252.
[46] P.W. Voorhees, J. Stat. Phys. 38 (1985) 231–252.
[47] M. Mujahid, J. Martin, J. Mater. Sci. Lett. 13 (1994) 153–155.
[48] A.P. Jirandehi, M. Mehdizadeh, M. Khonsari,Int. J. Mech. Sci. 176 (2020), 105525.
[49] S. Li, Z. Zhou, P. Wang, H. Sun, M. Wang, G. Zhang, Mater. Des. 90 (2016) 318–329.
[50] M. Wang, Z. Zhou, H. Sun, H. Hu, S. Li, J. Nucl. Mater. 430 (2012) 259–263.
[51] T.-K. Kim, C.-S. Bae, D.-H. Kim, J.-S. Jang, S.-H. Kim, C.-B. Lee, D.-H. Hahn, Nucl. Eng. Technol. 40 (2008) 305–310.
[52] R.L. Klueh, J.P. Shingledecker, R.W. Swindeman, D.T. Hoelzer, J. Nucl. Mater. 341 (2005) 103–114.
[53] P. Koncz, Á. Horváth, K. Balázsi, F.Ç. Şahin, G. Göller, Y. Onüralp, C. Balázsi, Mater. Sci. Forum 729 (2012) 409–414.
[54] S. Pasebani, A.K. Dutt, J. Burns, I. Charit, R.S. Mishra, Mater. Sci. Eng. A 630 (2015) 155–169.

[55] A.K. Mukherjee, J.E. Bird, J.E. Dorn, Experimental Correlations for High-temperature Creep, California, 1968.
[56] C. Phaniraj, M. Nandagopal, S. Mannan, P. Rodriguez, Acta Metall. Mater. 39 (1991) 1651–1656.
[57] N.E. Dowling, Mechanical Behavior of Materials: Engineering Methods for Deformation, Fracture, and Fatigue, Pearson Education Limited, 2012.
[58] C. Phaniraj, K. Samuel, S. Mannan, P. Rodriguez, International Conference on Creep, JSME, Tokyo, 1986, pp. 205–208.